AMOC stability and diverging response to Arctic sea ice decline in two climate models

Hui Li, Alexey V. Fedorov, Wei Liu

AMOC Stability and Diverging Response to Arctic Sea Ice Decline in Two Climate Models

HUI LI,[a] ALEXEY FEDOROV,[b,c] AND WEI LIU[d]

[a] *Climate and Global Dynamics, National Center for Atmospheric Research, Boulder, Colorado*
[b] *Department of Geology and Geophysics, Yale University, New Haven, Connecticut*
[c] *LOCEAN/IPSL, Sorbonne University, Paris, France*
[d] *Department of Earth and Planetary Sciences, University of California Riverside, Riverside, California*

(Manuscript received 24 July 2020, in final form 25 March 2021)

ABSTRACT: This study compares the impacts of Arctic sea ice decline on the Atlantic meridional overturning circulation (AMOC) in two configurations of the Community Earth System Model with different horizontal resolution. In a suite of model experiments, we impose radiative imbalance at the ice surface, replicating a loss of sea ice cover comparable to that observed during 1979–2014, and we find dramatic differences in the AMOC response between the two models. In the lower-resolution configuration, the AMOC weakens by about one-third over the first 100 years, approaching a new quasi-equilibrium. By contrast, in the higher-resolution configuration, the AMOC weakens by ~10% during the first 20–30 years followed by a full recovery driven by invigorated deep water formation in the Labrador Sea and adjacent regions. We investigate these differences using a diagnostic AMOC stability indicator, which reflects the AMOC freshwater transport in and out of the basin and hence the strength of the basin-scale salt-advection feedback. This indicator suggests that the AMOC in the lower-resolution model is less stable and more sensitive to surface perturbations, as confirmed by hosing experiments mimicking Arctic freshening due to sea ice decline. Differences between the models' mean states, including the Atlantic Ocean mean surface freshwater fluxes, control the differences in AMOC stability. Our results demonstrate that the AMOC stability indicator is indeed useful for evaluating AMOC sensitivity to perturbations. We emphasize that, despite the differences in the long-term adjustment, both models simulate a multidecadal AMOC weakening caused by Arctic sea ice decline, relevant to climate change.

KEYWORDS: Atlantic Ocean; Sea ice; Ocean circulation; Climate models

1. Introduction

Variations in the Atlantic meridional overturning circulation (AMOC) are critical for global and regional climate, as this ocean circulation plays a key role in sequestering heat and carbon into the deep ocean and regulating global ocean heat transport (e.g., Kostov et al. 2014; Marshall et al. 2014; Trenberth and Caron 2001; Liu et al. 2020). Paleo-proxy records suggest that AMOC variation and possible collapse were responsible for rapid swings of temperature in the past [Broecker et al. 1990; Dansgaard et al. 1993; see Lynch-Stieglitz (2016) for a review]. Recent observations of AMOC strength at 26.5°N by the RAPID arrays (Smeed et al. 2018) suggest a downward trend, but the nature of this AMOC slowdown remains unclear (e.g., Booth et al. 2012; Caesar et al. 2018; Rahmstorf et al. 2015).

Meanwhile, Arctic sea ice has been declining over the past few decades. The summer minimum sea ice extent shows a decreasing trend of 13.4% per decade from 1979 to 2020. Recent studies have found that the Arctic sea ice extent and the AMOC are closely connected and exhibit two-way interactions (Liu and Fedorov 2021, manuscript submitted to *npj Climate Atmos. Sci.*). Multidecadal variability of the summer Arctic sea ice extent is significantly correlated with the Atlantic multidecadal variability (AMV) and the ocean heat transport by the AMOC (Zhang 2015; Day et al. 2012; Miles et al. 2014; Mahajan et al 2011). Meanwhile, the decreasing Arctic sea ice can contribute to the AMOC slowdown by inducing warm and fresh surface anomalies that could spread into the subpolar region on multidecadal time scales (Liu et al. 2018; Sévellec et al. 2017; Sun et al. 2018), suppressing deep convection over the North Atlantic Deep Water (NADW) formation sites. The goal of this paper is to compare and contrast the response of the AMOC to such buoyancy anomalies in two configurations of the same fully coupled model.

Understanding the AMOC response to buoyancy forcing is complicated by the salt-advection feedback (Stommel 1961), which can create a positive loop in the context of ongoing climate change; that is, a weakening of the AMOC would reduce northward salt transport reaching the deep convection sites and subsequently weakens the AMOC even more. In this framework, the AMOC may collapse, possibly transitioning to another equilibrium state. This multi-equilibrium behavior of the AMOC has been examined extensively across models of various complexities [Jackson et al. 2017; Manabe and Stouffer 1999; Rahmstorf 1996; Rahmstorf et al. 2005; Yin and Stouffer 2007; Liu and Liu 2013; see Weijer et al. (2019) for a review], focusing on whether the AMOC is mono- or bistable.

Rahmstorf (1996) first proposed that AMOC stability can be inferred from M_{ovS}—that is, freshwater transport by the overturning circulation across the southern boundary of the Atlantic Ocean basin—and M_{ovS} was then used as an AMOC stability indicator (de Vries and Weber 2005), which was later refined as the Atlantic freshwater divergence (Dijkstra 2007; Huisman et al. 2010; Liu and Liu 2013). A positive M_{ovS} implies freshwater convergence into the Atlantic basin: a weakening of the AMOC would lead to less freshwater convergence and increased Atlantic salinity strengthening the circulation, thus creating a negative feedback and a monostable AMOC. A negative M_{ovS} would mean that the AMOC exports freshwater from the North Atlantic: a weakening of the AMOC would lead to accumulation of freshwater in the North Atlantic, which would result in a positive feedback further weakening the AMOC, implying a bistable

Corresponding author: Hui Li, huili7@ucar.edu

DOI: 10.1175/JCLI-D-20-0572.1

AMOC. Many fully coupled general circulation models (GCMs) appear to exhibit a monostable AMOC (Stouffer et al. 2006; Yin and Stouffer 2007), but they may have a bias toward being overly stable (Drijfhout et al. 2011; Liu et al. 2017).

GCMs consistently project a weakening of the AMOC under future global warming scenarios (Gregory et al. 2005), but the projected magnitude and time scale of such weakening vary considerably (Buckley and Marshall 2016; Weaver et al. 2012). The wide spread of AMOC response to external forcing among models may in fact be related to AMOC stability characteristics (Liu et al. 2014, 2017; Stouffer et al. 2006), which can depend on model properties, particularly ocean vertical mixing parameterization (Gent 2018; Prange et al. 2003; Sijp and England 2006), air–sea boundary conditions (Bryan 1986; Danabasoglu et al. 2014), and model resolution (Bryan et al. 2007).

Here we aim to examine the AMOC response to transient buoyancy forcing induced by Arctic sea ice decline in two models with different horizontal resolution and investigate how the different behaviors can be related to the AMOC stability properties. A deeper understanding of AMOC sensitivity to Arctic sea ice decline can help better quantify how the AMOC will change in a warming climate and assess the associated impacts and feedbacks to the climate system itself. Note that here we focus on the transient response of the AMOC on multidecadal to centennial time scales, which is different from the equilibrium response, and we define the stability of the AMOC in terms of its response to surface flux perturbations rather than to initial disturbances.

The paper is structured as follows. Section 2 describes the observational data, model configurations, and the AMOC stability indicator. Section 3 describes the main results, which are organized into five parts: the simulated Arctic sea ice decline and associated AMOC changes (section 3a), the AMOC stability indicator and salt-advection feedback (section 3b), comparison to freshwater hosing experiments (section 3c), and the mechanisms behind the different AMOC behaviors, including differences in surface freshwater fluxes (section 3d) and the NADW formation (section 3e). The key findings of the paper are discussed and summarized in section 4.

2. Observations, model experiments, and the AMOC stability indicator

a. Observational data

The observed historical sea ice extent from 1979 to 2014 is obtained from the National Snow and Ice Data Center (NSIDC). Sea ice volume for the same time period is provided by the Pan-Arctic Ice Ocean Modeling and Assimilation System (PIOMAS). The observation-based ocean data are from the operational ocean analysis/reanalysis system version 4 (ORAS4) ocean reanalysis by the European Centre for Medium-Range Weather Forecasts (ECMWF). ORAS4 has a horizontal resolution of 1° with equatorial refinement of 0.3°. It has 42 vertical levels with 10–15-m level thickness in the upper 200 m (Balmaseda et al. 2013). We use the period of 1970–2000 for climatology calculations.

b. Model experiments

The model experiments are performed with Community Earth System Model, version 1 (CESM1) (Hurrell et al. 2013). We adopt two model configurations that differ in model resolution: a ''low res'' experiment (T31_gx3v7) and a ''high res'' experiment (f09_gx1v6). In the low-res experiment, the atmosphere (CAM4) and land component (CLM4) use a nominal ~3.75° horizontal grid spacing, while the ocean (POP2) and sea ice component (CICE4) use a nominal ~3° horizontal grid spacing. In the high-res experiment, the grid spacing is ~2° for atmosphere and land and ~1° for the ocean and sea ice. Both versions of the ocean model use the Greenland pole grid, which has finer grid spacings near the subpolar North Atlantic and the Arctic. The two models also use similar parameterizations of ocean mixing. Note that *high res* here is a relative term, as this is in fact a typical resolution used in CMIP5 models.

Besides the resolution, there are several key differences between the models (e.g., Shields et al. 2012). For example, the low-res model uses a T31 spectral dynamical core for the atmospheric and land components while the high-resolution model applies a finite-volume dynamical core for atmosphere. The two models use different cloud parameter settings in the atmosphere model component to achieve radiative balance. A turbulent mountain stress parameterization is included in the low-res model. Ice albedo and some ocean parameter settings in the ice and ocean components, respectively, are also different.

Together, all of the above differences between the two models result in different strengths of the AMOC [17 Sv (1 Sv $\equiv 10^6\,\mathrm{m^3\,s^{-1}}$) in the low-res vs 24 Sv in the high-res], different spatial structure of the regions of deep convection, and different model biases. Consequently, we could consider these GCMs as two different models, albeit of the same model family. For brevity, however, we will still refer to these models as the high- and low-resolution models.

We perform a suite of sea ice perturbation experiments in which we reproduce the observed amount of sea ice melting during 1979–2014 by perturbing radiative balance at the sea ice surface. In both versions of the model, we conduct simulations under the preindustrial climate conditions and modify the albedo of Arctic sea ice to increase the absorption of shortwave radiation. Modifying the sea ice surface albedo allows us to alter sea ice extent while maintaining overall ocean–atmosphere energy balance. The resultant ice changes involve the classical ice-albedo feedback: the melting of sea ice caused by the imposed albedo reduction occurs largely on the margins of Arctic sea ice, where the ice cover is being replaced by open water, which strongly increases the absorption of solar radiation by the ocean, leading to the further loss of sea ice.

We modify the sea ice albedo by changing the optical properties of snow, bare sea ice, and ponded ice over the Arctic area within the model sea ice component. The modification is applied in the delta-Eddington solar radiation treatment within the model sea ice component. For the low-res model, we adjust the optical properties of bare ice and ponded ice by changing the standard deviation parameters (R_ice and R_pnd) from 0 to −2. In addition, the single scattering albedo (the probability that a single event results in scattering) of snow is reduced by 10% for all spectral

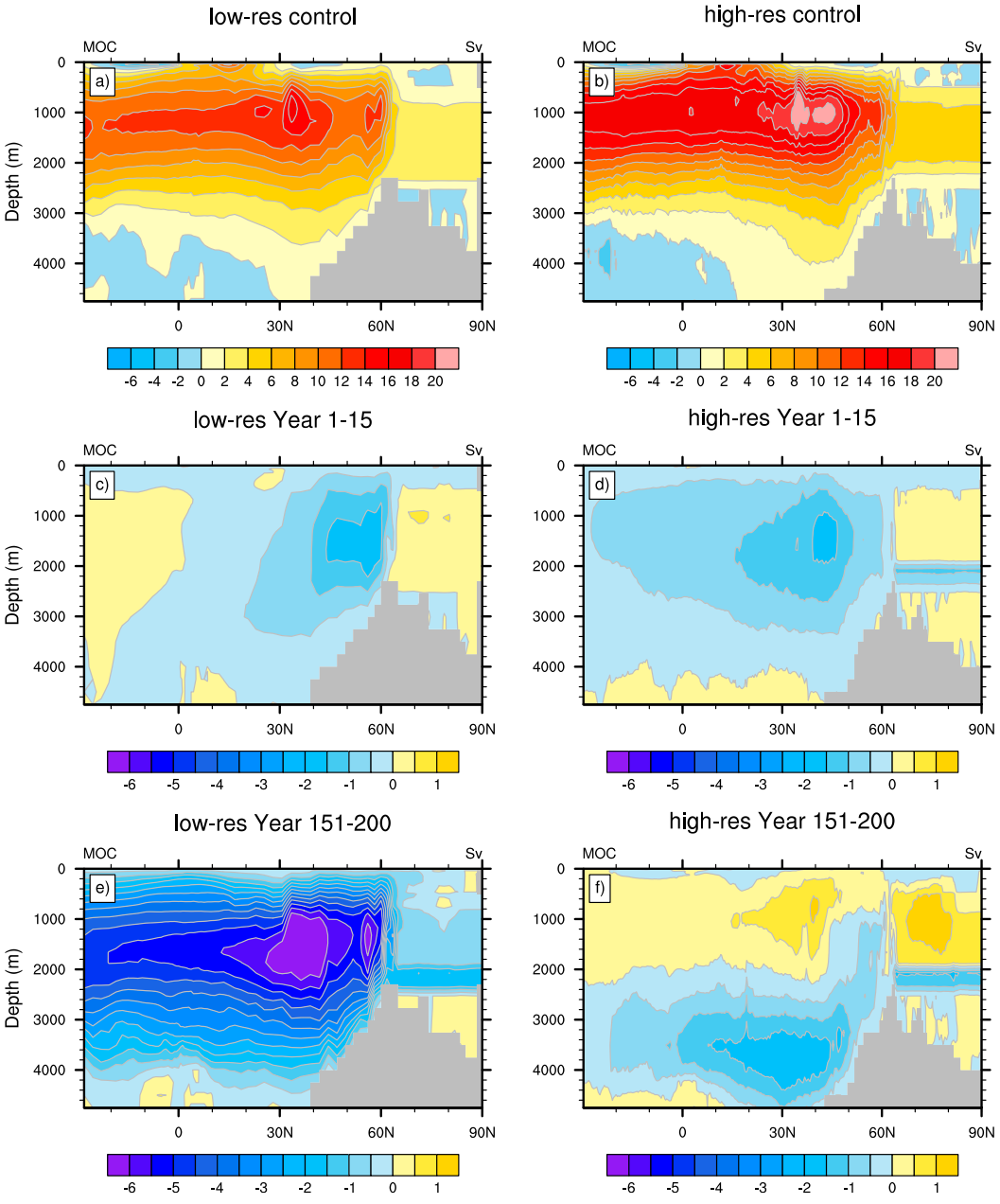

FIG. 1. (a),(b) Zonal mean Atlantic Ocean streamfunction (Sv) in the control experiment. (c)–(f) Anomalous streamfunction in the sea ice perturbation experiments for (left) low-res and (right) high-res simulations. The streamfunction anomalies are given for (middle) the initial phase of the experiments (years 1–15; the AMOC weakens in both models) and (bottom) the quasi-equilibrium phase (years 151–200; the AMOC weakens further in the low-res model but recovers in the high-res model).

bands. The low-res experiment has 10 ensemble members with the same albedo modifications. For the high-res model, we conducted three experiments with slightly different albedo modifications, where R_ice and R_pnd are changed from 0 to −3, −4, and −5, respectively. The three experiments produced very similar sea ice decline and a robust AMOC response, and we therefore regard the high-res experiments as a small ensemble. In both models, the sea ice albedo perturbation is applied at time zero and maintained for 200 years.

We also perform a set of freshwater hosing experiments, in which we add freshwater forcing uniformly over the North Atlantic Ocean between 50°–70°N in both versions of the model. The additional freshwater is compensated by subtracting the equivalent amount from the rest of the global ocean. The forcing is applied continuously over the 200 years as

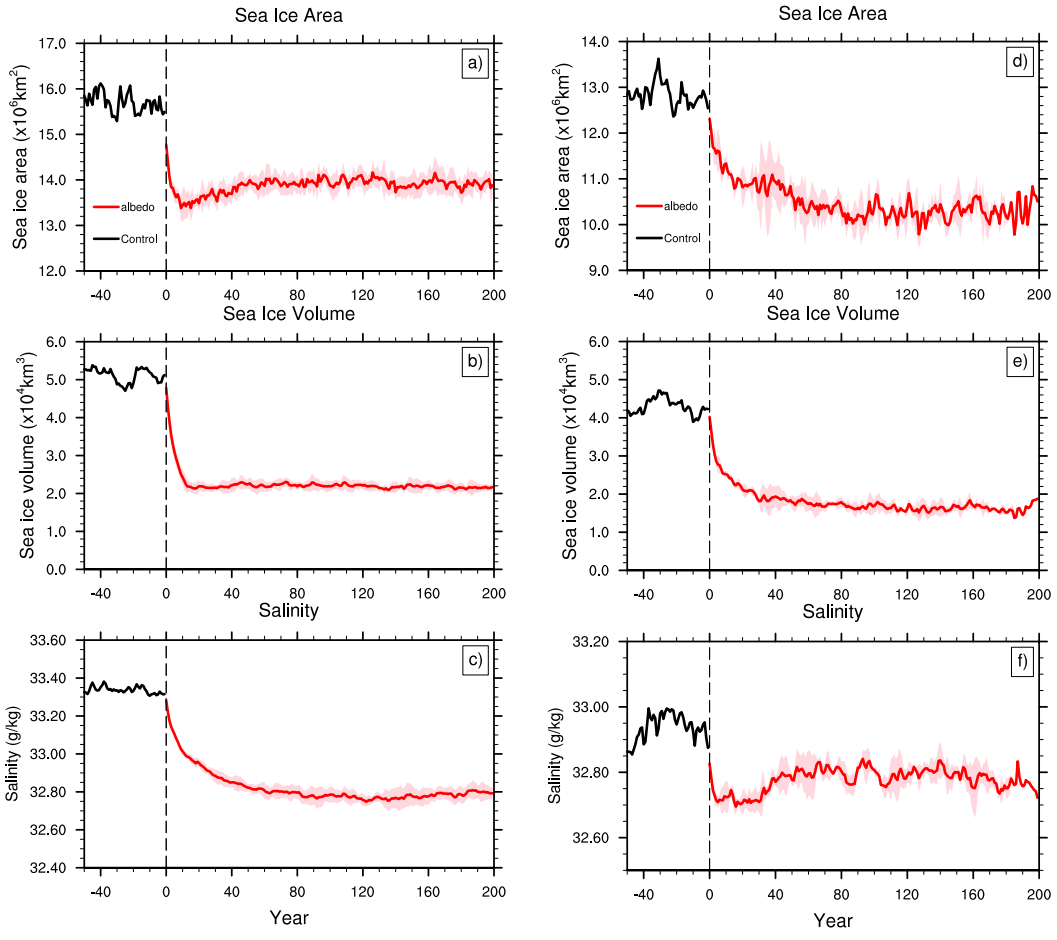

FIG. 2. Arctic Ocean annual mean (a),(d) sea ice total area, (b),(e) sea ice volume, and (c),(f) average upper-ocean salinity (0–300-m depth; 60°–90°N) in the (left) low-res and (right) high-res perturbation experiments (red lines). Shading represents ensemble spread (1 standard deviation). Year 0 marks the initiation of perturbation to sea ice radiative balance. The last 50 years of the control simulations (before year 0) are shown in black.

in the sea ice perturbation experiment. We conduct these experiments for the magnitudes of freshwater hosing of 0.05, 0.08, and 0.1 Sv.

The AMOC strength in the experiments is computed as the annual mean streamfunction maximum below 500 m in the North Atlantic. While in the control simulation the climatological mean AMOC is stronger in the high-res than in the low-res experiment, the two models simulate generally similar structures of AMOC streamfunctions (Fig. 1).

c. *AMOC stability indicator*

We adopt the AMOC stability indicator proposed in previous studies (Dijkstra 2007; Huisman et al. 2010; Liu and Liu 2013; Liu et al. 2017). In many studies it was used in the context of the AMOC being bistable or monostable when subjected to surface freshwater forcing [see Weijer et al. (2019) for a review]. Here, we explore whether this indicator can provide information of the AMOC transient sensitivity to surface perturbations. The AMOC stability indicator is defined as freshwater convergence by the baroclinic flow and combines freshwater transports at the Atlantic southern (~34°S; M_{ovS}) and northern (~80°N; M_{ovN}) boundaries:

$$\Delta M_{\mathrm{ov}} = M_{\mathrm{ovS}} - M_{\mathrm{ovN}}. \tag{1}$$

The northern boundary consists of three vertical sections: across the Canadian Arctic Archipelago, the Fram Strait, and the western shelf of the Barents Sea.

The freshwater transport by the overturning circulation is defined as

$$M_{\mathrm{ovS,N}} = -\frac{1}{S_0}\int_{-D}^{0} \overline{v^*}(z)\langle S(z) - S_0\rangle \, dz, \tag{2}$$

where S_0 denotes a reference salinity of 34.8 psu, z denotes the vertical coordinate, $-D$ represents the ocean depth, $v^*(z)$ is the baroclinic component of meridional ocean velocity at the northern or southern boundaries, the angle brackets denote zonal average, and the overbar indicates zonal integration.

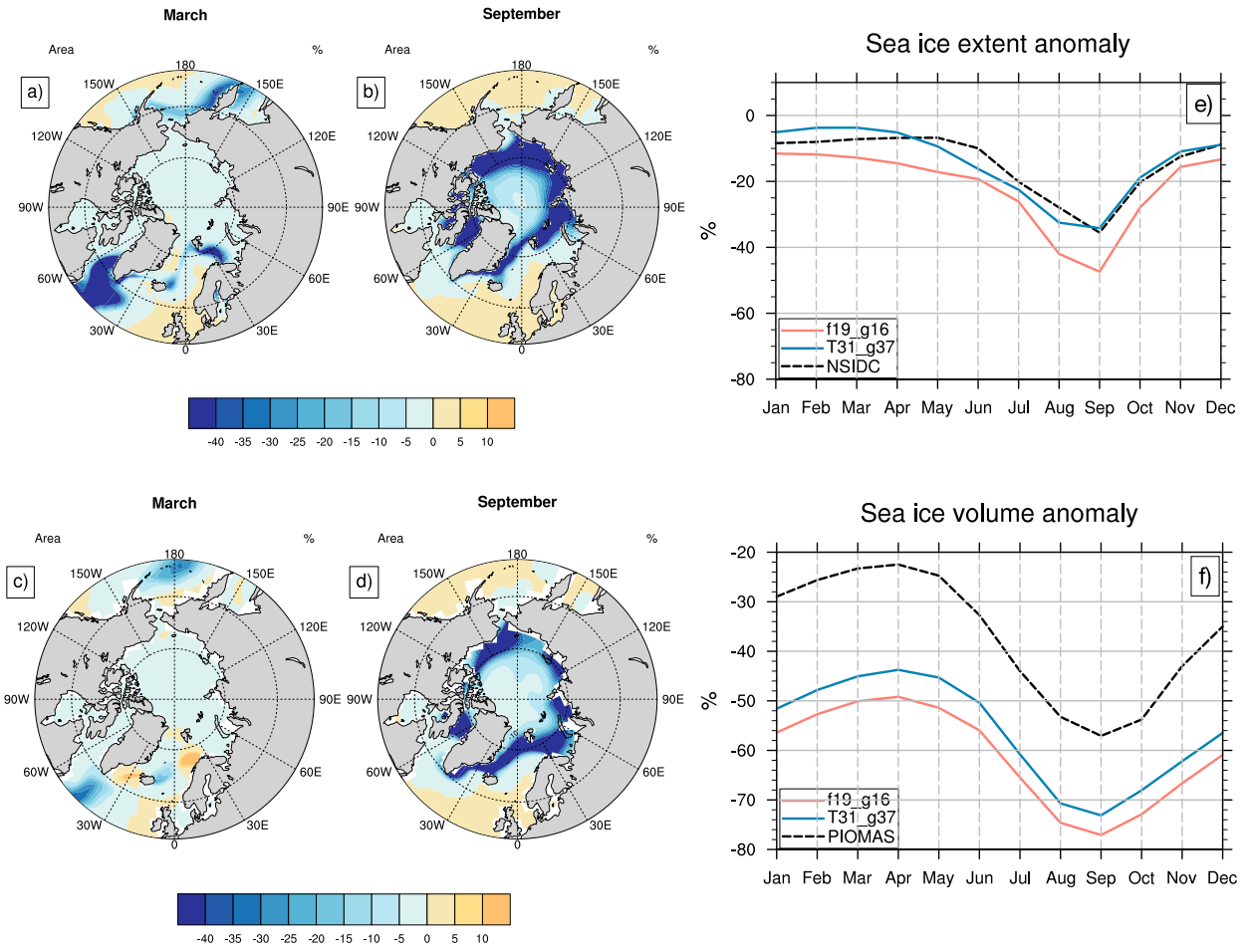

FIG. 3. Sea ice concentration anomalies (%) in (left) March and (center) September simulated in the (a),(b) high-res and (c),(d) low-res sea ice perturbation experiments. Ensemble means are used. Also shown are relative changes in the seasonality of (e) sea ice extent and (f) volume in the low-res (blue) and high-res (red) models as compared with the observed changes (dashed black line). The modeled anomalies are defined as the mean difference between the last 50 years of the perturbation simulations and the last 50 years of the respective control. Anomalies in the observations are defined as the mean difference between 2005–14 and 1979–88. The perturbation experiments reproduce well the observed reduction in Arctic sea ice extent but overestimate the reduction in sea ice volume.

The azonal transports at the southern and the northern boundaries, which account for the transport by gyre circulations, is defined as

$$M_{\mathrm{azS,N}} = -\frac{1}{S_0}\int_{-D}^{0} \overline{v'(z)S'(z)}dz, \tag{3}$$

where $v(z)$ is the full meridional ocean velocity. The prime represents deviations from the zonal mean. The total freshwater transport by gyre circulation is therefore

$$\Delta M_{\mathrm{az}} = M_{\mathrm{azS}} - M_{\mathrm{azN}}. \tag{4}$$

3. Results

a. Sea ice decline experiments

Figure 2 shows the generated changes in Arctic total sea ice area and volume in the two models. The climatological annual mean total Arctic sea ice cover in the high-res control simulation is roughly $12.8 \times 10^6\,\mathrm{km}^2$, which agrees with the observations during the 1980s. The simulated sea ice volume of $4 \times 10^4\,\mathrm{km}^3$, however, is larger than the observed estimates ($\sim 2.6 \times 10^4\,\mathrm{km}^3$), owing to overestimated sea ice thickness in the model. Total sea ice area and volume are both larger in the low-res model than in the high-res model. Shortly after the radiative perturbation is activated, both models show rapid sea ice decline in the first 10 years. Sea ice in the low-res model then stabilizes and persists for the rest of the 200 years, whereas sea ice in the high-res model undergoes a gradual adjustment before reaching a new balance at ~year 80. By the time of new equilibration, the total sea ice area in the low-res (high-res) model reduces by $2 \times 10^6\,\mathrm{km}^2$ ($2.5 \times 10^6\,\mathrm{km}^2$), and the total sea ice volume in the low-res (high-res) model reduces by $2.8 \times 10^4\,\mathrm{km}^3$ ($2.7 \times 10^4\,\mathrm{km}^3$). Thus, the two models lose approximately the same amount of sea ice.

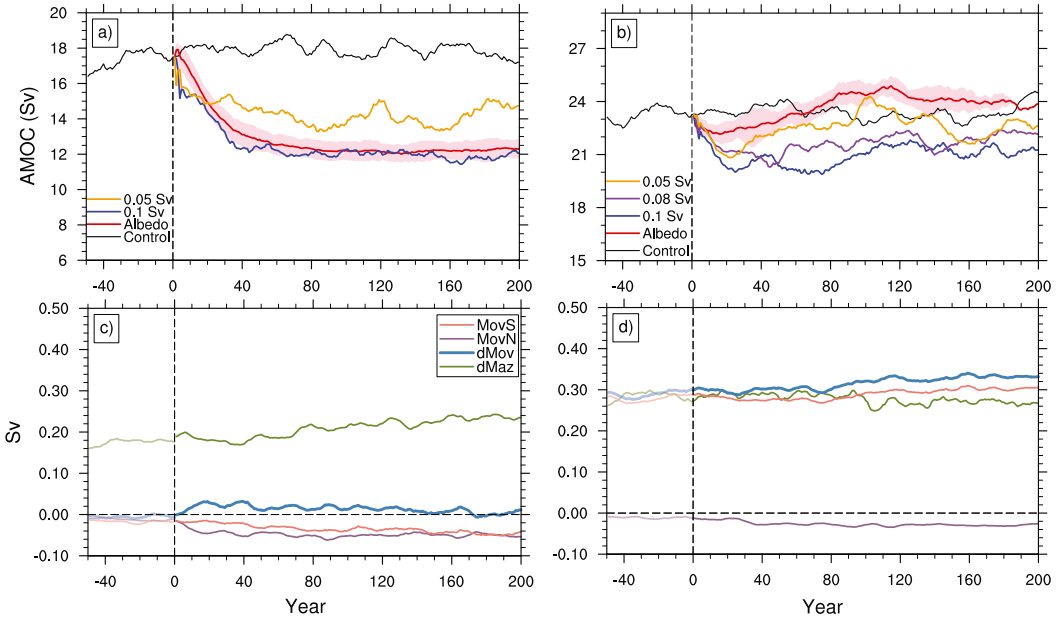

FIG. 4. AMOC strength (Sv) in the (a) low-res and (b) high-res simulations as a function of time. Black curves show the respective control, and red curves show AMOC responses to sea ice decline in the sea ice perturbed simulations. Pink shading represents ensemble spread (1 standard deviation). Results are compared with hosing experiments with 0.1-Sv (blue), 0.08-Sv (purple), and 0.05-Sv (orange) freshwater forcing. The result for the low-res 0.08-Sv hosing experiment is not shown, because it is very similar to the 0.1-Sv forcing. Also shown is the ensemble mean time series of the AMOC stability indicator (ΔM_{ov}; steel blue), freshwater transport by overturning at 34°S (M_{ovS}; salmon pink) and at the northern boundaries (M_{ovN}; plum), and total azonal transport (ΔM_{az}, green) in the (c) low-res and (d) high-res sea ice perturbed simulations. $\Delta M_{ov} = M_{ovS} - M_{ovN}$. All time series are smoothed with a 10-yr running mean. Note that the AMOC stability indicator stays close to zero for the low-res configuration but is strongly positive for the high-res model.

Meanwhile, the upper ocean (0–300 m) in the Arctic and sub-Arctic region becomes fresher over time (Figs. 2c,f). In the low-res model, the average Arctic Ocean salinity in the upper 300 m decreases by 0.55 psu, which is much larger than the equivalent freshening due to the initial sea ice melting alone. Li and Fedorov (2021, manuscript submitted to *npj Climate Dyn.*) find that this anomalous freshening occurs through a distillation-like process associated with seasonal sea ice melting that freshens the upper ocean while mean overturning circulation removes excess salt from the region. This freshening mechanism is also present in the high-res model, although the magnitude of the anomalous freshening is smaller.

The two models show consistent changes of sea ice seasonality, although the high-res has a slightly higher percentage reduction than the low-res (Figs. 3e,f). Since the two models simulate larger sea ice volume than the observed, here we focus on the relative changes to obtain a clearer comparison of seasonality changes. Both models show significant melting along sea ice margins in summer (Figs. 3b,d) and a reduction of sea ice cover in the subpolar gyre in winter. The low-res model shows anomalous winter sea ice growth in the Denmark Strait and the Norwegian Sea, along the path of the North Atlantic inflow water, which is contrary to the pattern in the high-res. As we will show next, this discrepancy can be attributed to different responses of the AMOC to buoyancy forcing induced by sea ice decline.

Within 10 years after the radiative perturbation is applied, the AMOC strengths in both models start to decrease (Figs. 4a,b), red curves). In the low-res model, the AMOC slowly adjusts for ~100 years before reaching a new equilibrium. At the end of the simulation, the total reduction of AMOC strength is 5 Sv, accounting for ~30% of change. In the high-res model, however, the AMOC weakens in the first 20 years but shortly after starts to recover. It then slowly returns to its initial strength over the following ~50 years. The maximum weakening at year 20 is ~2 Sv, which is less than 10% of change. At the end (years 151–200), a strengthened clockwise circulation is evident in the upper 2000 m, corresponding to AMOC recovery and slight intensification (Fig. 1f). In addition, there has emerged an anomalous counterclockwise pattern at 1000-m depth at around 50°–60°N, concurrent with the intensification of the Arctic circulation north of 60°N, suggesting a latitudinal shift of the deep convection sites. This is also evident from surface freshwater flux anomalies (Fig. 5) and changes in winter mixed layer depth (Fig. 6). Changes in deep water formation that occur in different deep convection sites will be discussed further in section 3e.

Figure 7 shows the Atlantic upper-ocean (0–300 m) zonal-mean density, salinity, and temperature anomalies in the two

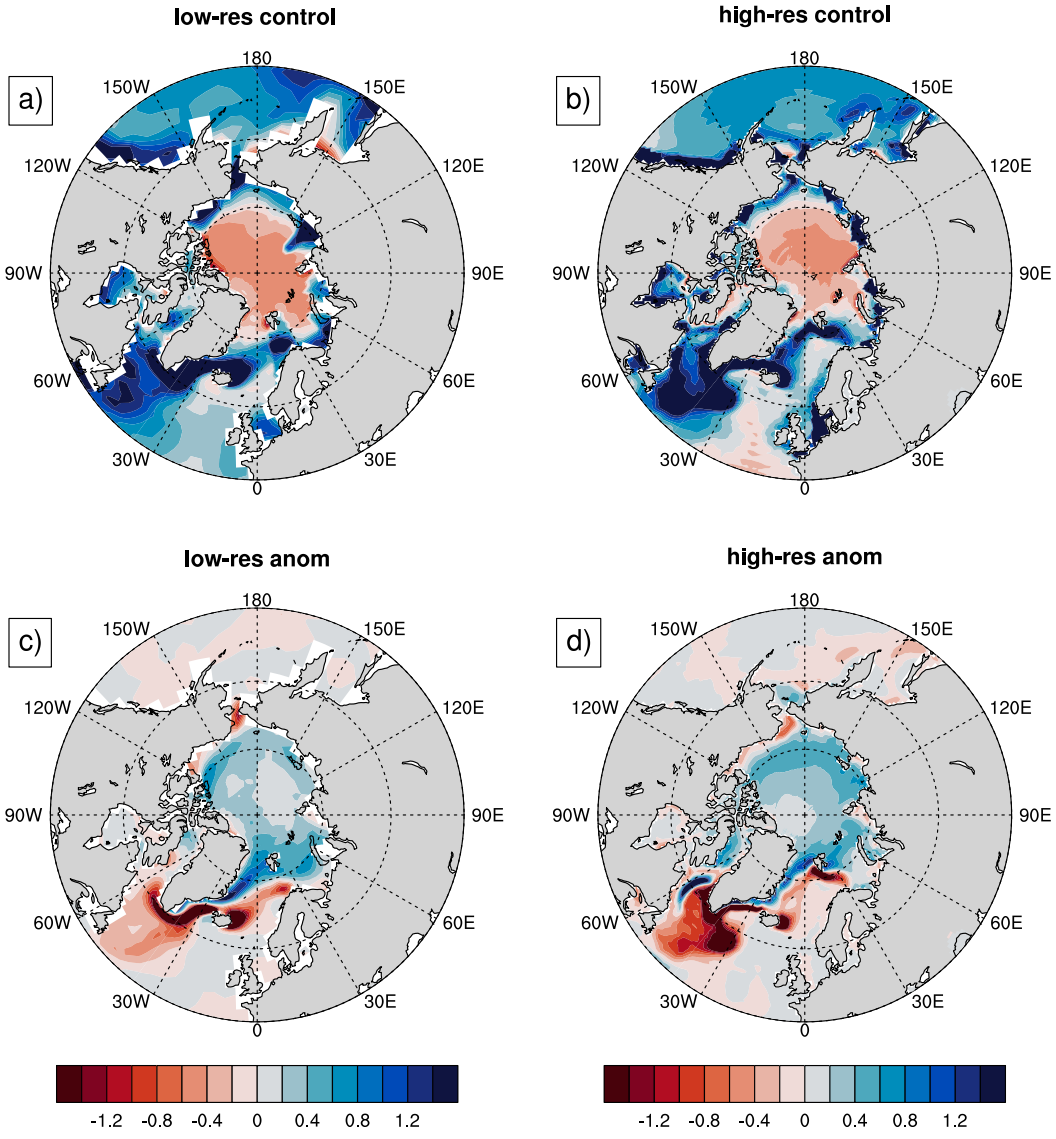

FIG. 5. Climatological mean surface freshwater fluxes (m yr^{-1}, positive into the ocean) in the (a),(c) low-res and (b),(d) high-res control simulations, Surface freshwater flux anomalies in the sea ice perturbation experiments are shown in (c) and (d) for each model, respectively. The anomalies are calculated using the mean of the last 50 years of each simulation.

models. The high-latitude upper oceans in both models show a persistent freshening and warming response to the sea ice albedo perturbation. The low-res model experiences a stronger decrease of salinity and density, and the freshening signal spreads farther south to 60°N after year 80. In the high-res model, however, the subpolar North Atlantic becomes saltier and warmer after year 60, corresponding to the recuperation and overshooting of the AMOC that transports more warm and saline water northward (Fig. 4b).

So far, we see that the two models experience similar amount of sea ice volume reduction and similar changes in ice seasonality, which indicates that the total freshwater forcing due to sea ice melting are comparable. However, the AMOC response diverges strongly: while the low-res model shows a robust 30% decrease followed by stabilization, the high-res model is resistant to the forcing and undergoes recovery within 80 years or less. What causes such a different AMOC response?

b. *AMOC stability and the salt-advection feedback*

The sensitivity of the AMOC to sea ice loss can be related to AMOC stability and the associated salt-advection feedback. Previous studies show that the majority of GCMs simulate an overly stable AMOC, making it more resistant to freshwater forcing (Stouffer et al. 2006; Hu et al. 2008; Liu et al. 2014). Here we examine AMOC stability properties in the two

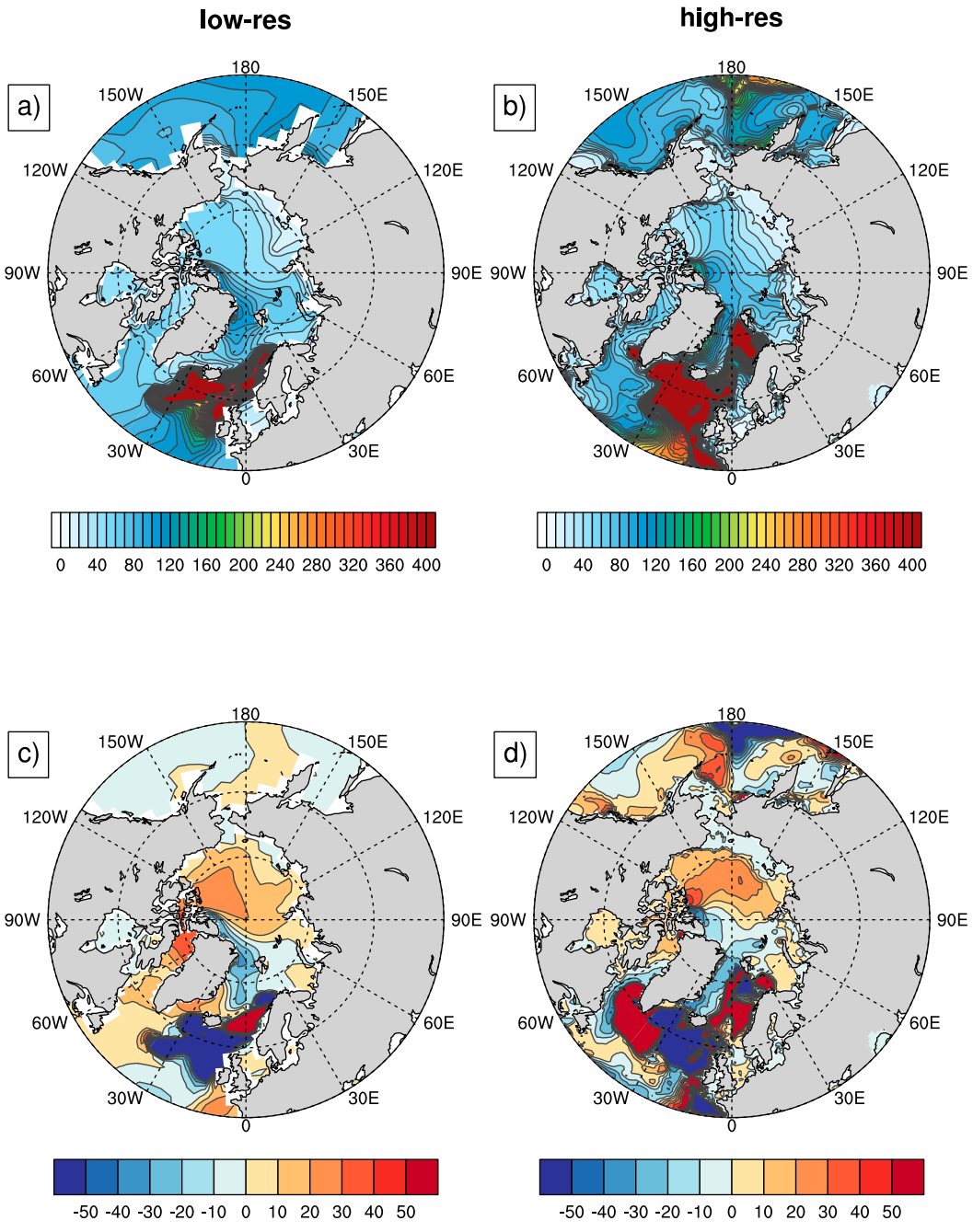

FIG. 6. Climatological mean March mixed layer depth (m) in the (a) low-res and (b) high-res control simulations. Mixed layer depth anomalies in the sea ice perturbation experiments are shown for the (c) low-res and (d) hi-res model. The anomalies are calculated using the mean of the last 50 years of each simulation. Note the deepening of the mixed layer in the Labrador Sea and in the region south of Greenland in the perturbation experiment with the high-res model, which points to the activation of deep convection there.

models using the diagnostic AMOC stability indicator, ΔM_{ov}. We consider both the equilibrated climate in the control runs and the transient changes in response to forcing.

We find that the long-term mean ΔM_{ov} in the low-res control simulation is -0.005 Sv (with $M_{ovS} = -0.017$ Sv and $M_{ovN} = -0.012$ Sv). The negative ΔM_{ov}, even of small magnitude, suggests that the overturning circulation tends to export freshwater out of the Atlantic catchment region. A reduction of AMOC strength will lead to anomalous freshwater accumulation that further weakens the circulation (a positive feedback). In contrast, the long-term mean ΔM_{ov} in the high-res model is ~ 0.28 Sv (with $M_{ovS} = 0.27$ Sv and $M_{ovN} = -0.01$ Sv). External freshwater forcing

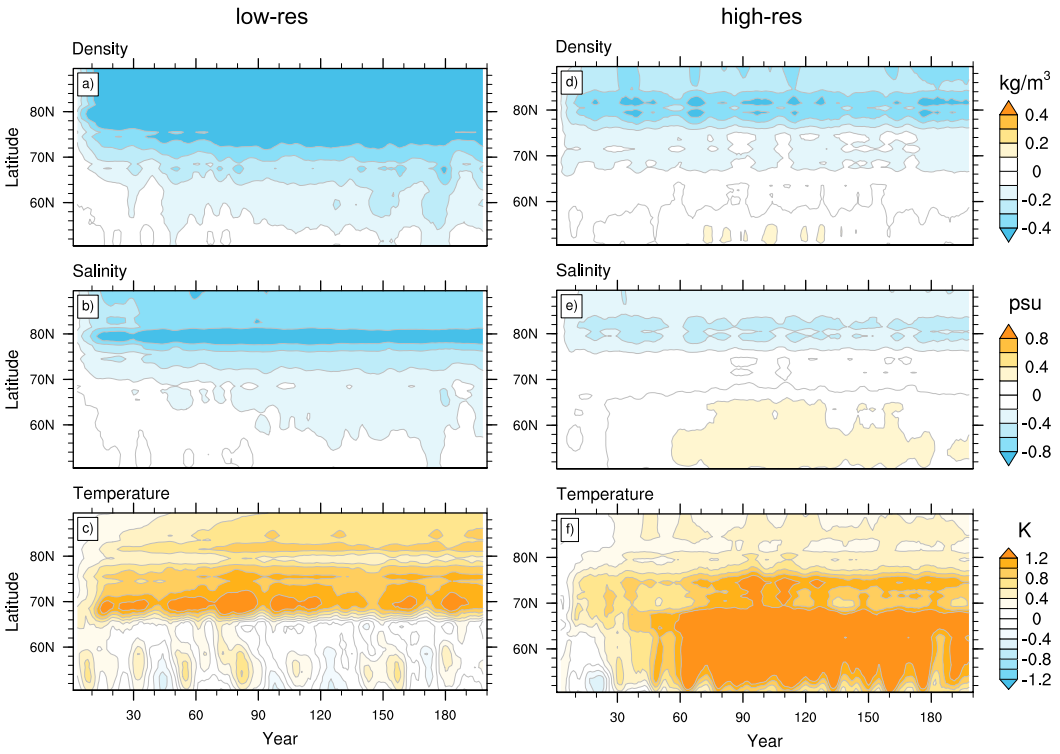

FIG. 7. Latitude–time plots of the Atlantic upper-ocean (0–300 m) annual mean anomalies in (a),(d) density, (b),(e) salinity, and (c),(f) temperature in the (left) low-res and (right) high-res sea ice perturbation experiments. These anomalies are zonally averaged and computed relative to the respective control simulations. Note that, in the high-res simulations, increased upper-ocean salt transport from midlatitudes by the AMOC counteracts the freshening signal coming from the Arctic.

can cause a damped "salt oscillation" due to the negative feedback (Broecker et al. 1990) without inducing an AMOC "off" state.

Figures 4c and 4d show the time series of ΔM_{ov}, M_{ovS}, M_{ovN}, and ΔM_{az} (as defined in section 2c) in the two models. In the low-res model, ΔM_{ov} rises very slightly above zero after the perturbation initiation, which is mainly due to the rapid southward spread of fresh meltwater across the northern boundaries (Fig. 4c, plum curve). Meanwhile, M_{ovS} gradually adjusts to the freshwater forcing by exporting more freshwater southward (Fig. 4c, salmon pink curve). The gyre transport ΔM_{az} enhances the freshwater convergence. Toward the end of the 200-yr simulation, the total overturning transport ΔM_{ov} slowly abates as the circulation adjusts to this abundance of freshwater and then stabilizes.

In the high-res model, ΔM_{ov} goes through relatively modest changes (Fig. 4d). Starting from about year 80, it slowly rises and reaches a relatively stable state of ~0.35 Sv by the end of the simulation. Note that when the AMOC starts to show signs of reintensification, ΔM_{ov} strengthens whereas the gyre component ΔM_{az} weakens. This shows a compensating effect of gyre transport to the reinvigoration of the AMOC. The AMOC response in the high-res model showcases the resistance of the system to external freshwater forcing.

The AMOC behavior in the sea ice perturbation experiments can be viewed as a combination of response (to sea ice forcing) and the resulting feedback. In the low-res, the AMOC is marginally unstable with small negative values of ΔM_{ov} (the long-term mean is −0.005 Sv). The freshwater forcing from sea ice melting and the positive large-scale salt-advection feedback by the AMOC work conjointly to reduce the AMOC strength. In contrast, in the high-res model, the AMOC salt-advection feedback has a damping effect on the freshening due to sea ice forcing.

Note that in the low-resolution model the AMOC stability indicator, while having generally negative values in the long-term control simulations, becomes slightly positive after the sea ice perturbation is imposed, which is mainly due to an increase in freshwater transport from the northern boundary (M_{ovN}). Then ΔM_{ov} wanders around zero as the system approaches equilibrium. This change helps prevent the AMOC from further weakening.

c. *Results from freshwater hosing experiments*

To further validate our hypothesis, we examine the response of the AMOC to freshwater forcing in the two models by conducting a suite of freshwater hosing experiments (Fig. 4). When exposed to a 0.1-Sv freshwater forcing (Figs. 4a,b, blue), the low-res AMOC response closely resembles the sea ice perturbation experiment with a 6-Sv reduction. In the high-res model, however, the AMOC response shows a weakening only in the first 80 years but then starts to recover. The final reduction

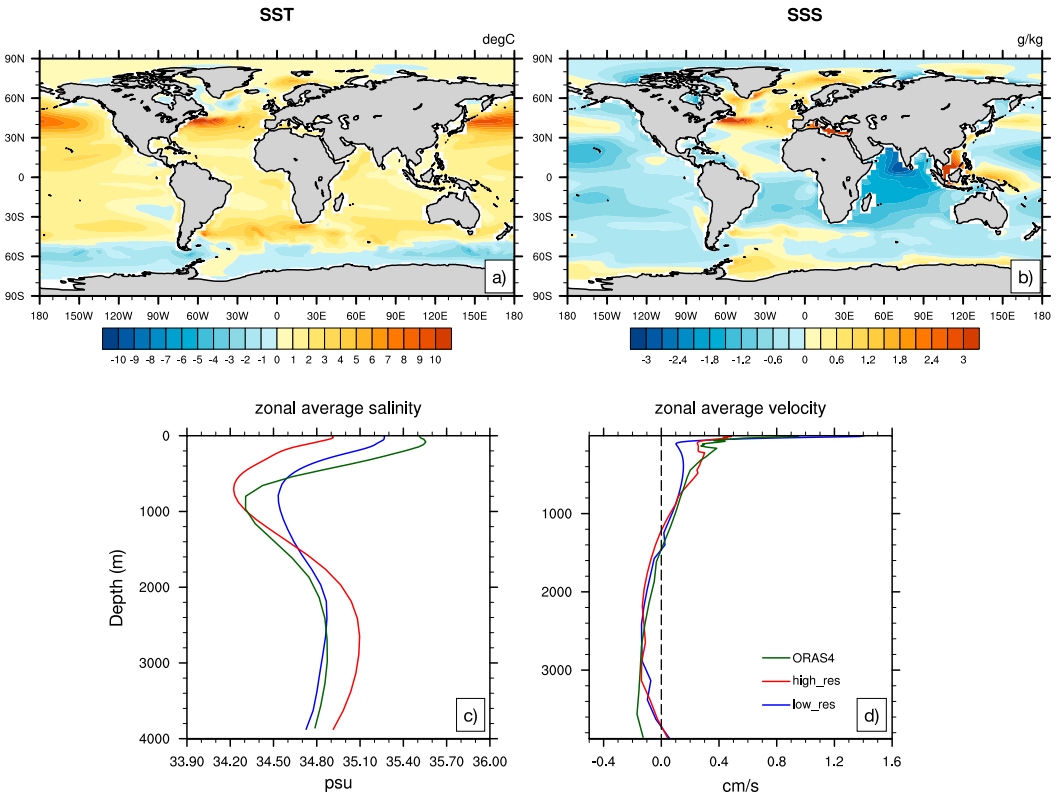

FIG. 8. Differences of long-term annual mean (a) SST and (b) SSS between the high-res and low-res controls (high-res minus low-res). Note that in the upper ocean the low-res model has a cold SST bias whereas the high-res has a low-salinity bias (except in the North Atlantic). Also shown are the vertical profiles of zonally averaged annual mean (c) salinity and (d) meridional velocity at the Atlantic southern boundary (34°S) in the low-res control (blue), the high-res control (red), and the ORAS4 ocean reanalysis for 1970–2000 (green). The low-resolution model gives a generally better agreement with the observed distribution of salinity.

of AMOC strength is ~2 Sv, representing only ~8% of change [a similar recovery was documented by Thomas and Fedorov (2019)]. Thus, the same buoyancy forcing has less of an impact on the AMOC strength in the high-res model than the low-res.

When the forcing rate is reduced by half to 0.05 Sv (Figs. 4a,b, orange), the low-res AMOC again shows a similar behavior as before, with the total weakening of roughly 3 Sv. Note that the AMOC in this simulation exhibits stronger variability. For the high-res model, a 0.05-Sv freshwater forcing produces a response not unlike the sea ice perturbation experiment, where the AMOC quickly subsides to the minimum strength within the first 30 years and then regains its strength in the following decades. The end result is an insignificant reduction, if any, that is almost indistinguishable from the AMOC interdecadal variability.

In the next two sections, we will explore the possible reasons behind the contrasting AMOC behaviors in the two models.

d. *Basinwide freshwater transport and the role of mean surface freshwater fluxes*

To understand the disparity in the AMOC stability indicator between the two models, we first look at the climatological annual mean sea surface temperature (SST), surface salinity (SSS), and vertical profiles of zonal average salinity and meridional velocity at 34°S in the two models (Fig. 8). On average, the high-res model has warmer and saltier Gulf Stream and North Atlantic Current waters, consistent with a stronger AMOC. At 34°S, the high-res model is fresher in the upper 1400 m than the low-res model; it is saltier below this depth. Such vertical distribution of salinity, combined with opposing meridional flows at these depths, induces an anomalously large northward freshwater transport into the Atlantic in the high-res model.

We further analyze the northward freshwater transport as a function of latitude in the Atlantic and investigate how this transport is related to freshwater flux at the ocean surface in the two models. The ocean freshwater content (FWC) tendency is determined by surface freshwater flux (SFC), convergence of freshwater transport (FT), and the diffusion term (DF): $d/dt(\mathrm{FWC}) = \mathrm{SFC} + \mathrm{FT} + \mathrm{DF}$. In a steady state, since the diffusion term is small, the total surface freshwater flux integrated from a given latitude to the Fram Strait should be roughly balanced by the northward freshwater transport across this latitude minus the northward freshwater transport through the Fram Strait (i.e., freshwater convergence, considering the Fram Strait

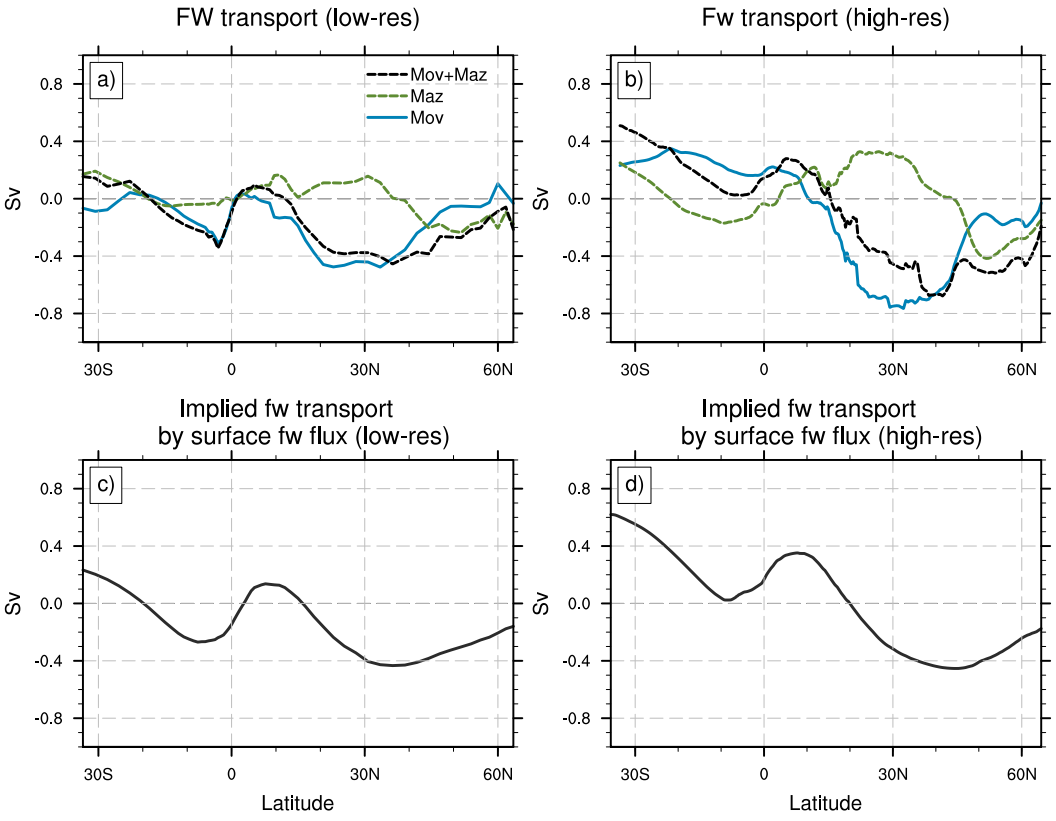

FIG. 9. (a),(b) Zonally integrated and depth-integrated freshwater transport in the Atlantic Ocean and its components associated with oceanic meridional overturning and horizontal (gyre) circulation (M_{ov} and M_{az}; Sv). (c),(d) Implied freshwater transport computed by integrating surface total freshwater flux (precipitation − evaporation + river runoff + ice melt − brine rejection) from the Fram Strait southward as a function of latitude, with the minus sign. The plots are shown for (left) the low-res model and (right) the high-res model.

as the northern boundary of the Atlantic basin). Note that the total freshwater transport through the Fram Strait is small, on the order of −0.01 Sv in both models, and therefore can be neglected.

Figure 9 shows the total northward freshwater transport FT and its components–freshwater transport by the meridional overturning circulation (M_{ov}) and by oceanic horizontal circulation (M_{az})–as well as the implied freshwater transport computed by integrating the total surface freshwater flux (which includes precipitation − evaporation + river runoff + ice melt − brine rejection) starting from the Fram Strait to 35°S (with the minus sign) in the two models. As expected, the total freshwater transport is approximately equal to the implied transport computed by integrating the total surface freshwater flux. Small differences between the direct and implied transports are largely due to the contribution from the diffusion terms.

We find that the total northward freshwater transport south of 40°N is dominated by M_{ov} in both models. The contribution of M_{az} becomes more important over the North Atlantic subpolar gyre. The M_{ov} and M_{az} terms have opposite signs over the North Atlantic subtropical gyre; M_{az} is generally stronger in the high-res model than in the low-res model. Meanwhile, we find that M_{ov} and the total freshwater transport in the higher-resolution model is positive and indeed large across the South Atlantic, meaning that the AMOC transports excess freshwater northward (Fig. 9b). This pattern of freshwater transport in the high-res model corresponds to a surface freshwater flux in the area north of 34°S that is much smaller than the low-res and the observational estimates (Bryden et al. 2011) (Fig. 9d), which we find is mainly due to too strong evaporation. Note that at the southern boundary (34°S), M_{az} is comparable between the two models, so that the difference in total freshwater transports is primarily due to M_{ov}. Thus, in the high-res model, the fact that M_{ov} at the southern boundary is positive is consistent with the need to transport more freshwater northward to compensate for the negative bias (excessive evaporation) in surface fluxes. This is in line with the conclusions of Mecking et al. (2017), who found that the salinity and surface flux bias in models can impact the sign of M_{ov}, and ultimately the AMOC bistability.

e. Water mass transformation and deep water formation in the North Atlantic

The NADW formation is an essential part of the AMOC, and we will now consider how it differs between the two model.

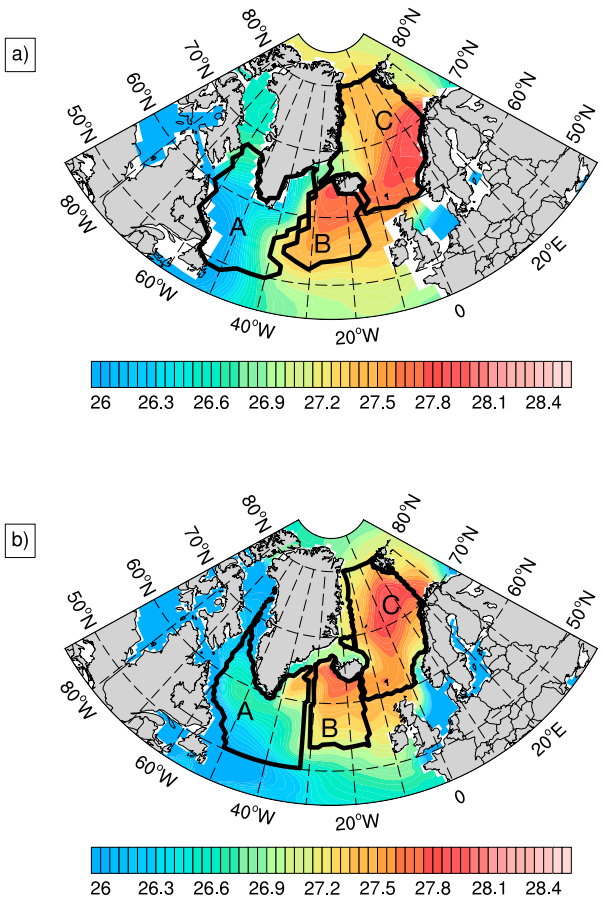

FIG. 10. Surface density (colors; kg m^{-3}) in the (a) low-res and (b) high-res control simulations. Solid black contours outline the three main regions of deep convection: region A is the broad Labrador Sea region, region B is the region south of Iceland, and region C is the Nordic seas. Note that the selected contours are slightly different between the two panels because the criteria for choosing the contours include both isopycnals and bathymetry, which differ between the two models.

As the March mixed layer depth indicates (Fig. 6), deep convection can potentially occur in these models in the region south of Iceland, in the Nordic seas, and possibly in a small part of the Labrador Sea (only for the high-res model). In the low-res model, deep convection in the Nordic seas is confined to an area stretched along the coast of Norway, and it is completely absent in the Labrador Sea. After the sea ice perturbation is imposed, deep convection in both models appears to decrease in the region south of Iceland, while in the Nordic seas the ocean mixed layer depth decreases in some areas but deepens in others. The largest difference in the response is seen over the Labrador Sea, where March mixed layer depth has increased dramatically but only in the high-res model.

To better understand the differences in NADW formation between the two models and their responses to the sea ice perturbation, we analyze water mass transformation in the potential regions of deep convection. Based on surface potential density, bathymetry, and winter mixed layer depth, the three major areas of deep convection are defined as the Labrador and Irminger Seas and the broad region south of Greenland (region A), the region south of Iceland (sometimes referred to as the Iceland Basin; region B), and the Nordic seas (region C) (Fig. 10). For brevity, we will refer to region A as the broad Labrador Sea region or simply the Labrador Sea.

Figure 11 shows water mass transformation rates [WMT; reviewed in Groeskamp et al. (2019)] within the three regions in the low- and high-res models, respectively. For each model, we compare WMT in the control and the sea ice perturbation simulations. Neutral density is binned by 0.05 kg m^{-3}. We find that, in the low-res model (Fig. 11, left panels), dense water is indeed formed within the region south of Iceland and in the Nordic seas but is absent in the broad Labrador Sea region. This is consistent with results inferred from the winter mixed layer depth. In the low-res sea ice perturbation experiment (Fig. 11, red curves in the left panels), both active convective regions shift toward less dense waters, but the Labrador Sea still shows no sign of dense water formation. In the high-res model (Fig. 11, right panels), WMT in the control simulation is similar to the low-res, with no dense water formation in the Labrador Sea (suggesting that ocean deep layer depth may not always be a good indicator of deep convection). However, in the perturbation experiment, there occurs a dramatic activation of dense water formation within the Labrador Sea. Meanwhile, WMT in the other two regions shifts toward less dense water, but the changes are smaller than in the low-res.

We further analyze the formation rates of dense water (Fig. 12) and their temporal changes in the two models (Fig. 13). The formation rate is the derivative of the WMT rate with respect to density, representing the creation (or destruction) of water within a certain density range. We focus on the formation rate for water denser than 27.7 kg m^{-3}, which represents here NADW. We find that, in the low-res control, the region south of Iceland and the Nordic seas region are of equal importance for deep water formation. Changes due to the imposed sea ice perturbation mainly affect the region south of Iceland, where the dense water formation rate decreases significantly over time, by nearly 6 Sv. The dense water formation rate decreases in the Nordic seas as well but only by about 2 Sv. No changes in the Labrador Sea are observed. In contrast, in the high-res model, the dense water formation rate starts to increase in the Labrador Sea at around year 15 and reaches the maximum around year 100. This is consistent with the evolution of the AMOC strength, suggesting that the activation of dense water formation in the Labrador Sea is critical for the AMOC recovery in the high-res model. While there is a slight decrease in dense water formation in the region south of Iceland, it is fully compensated by the strong increase in the Labrador Sea.

4. Discussion and conclusions

In this study, we have compared the AMOC response to a modeled sea ice decline that is comparable to the observed during the past three decades in two different configurations of CESM1. These two models differ in their horizontal resolution and several other important model properties. The AMOC

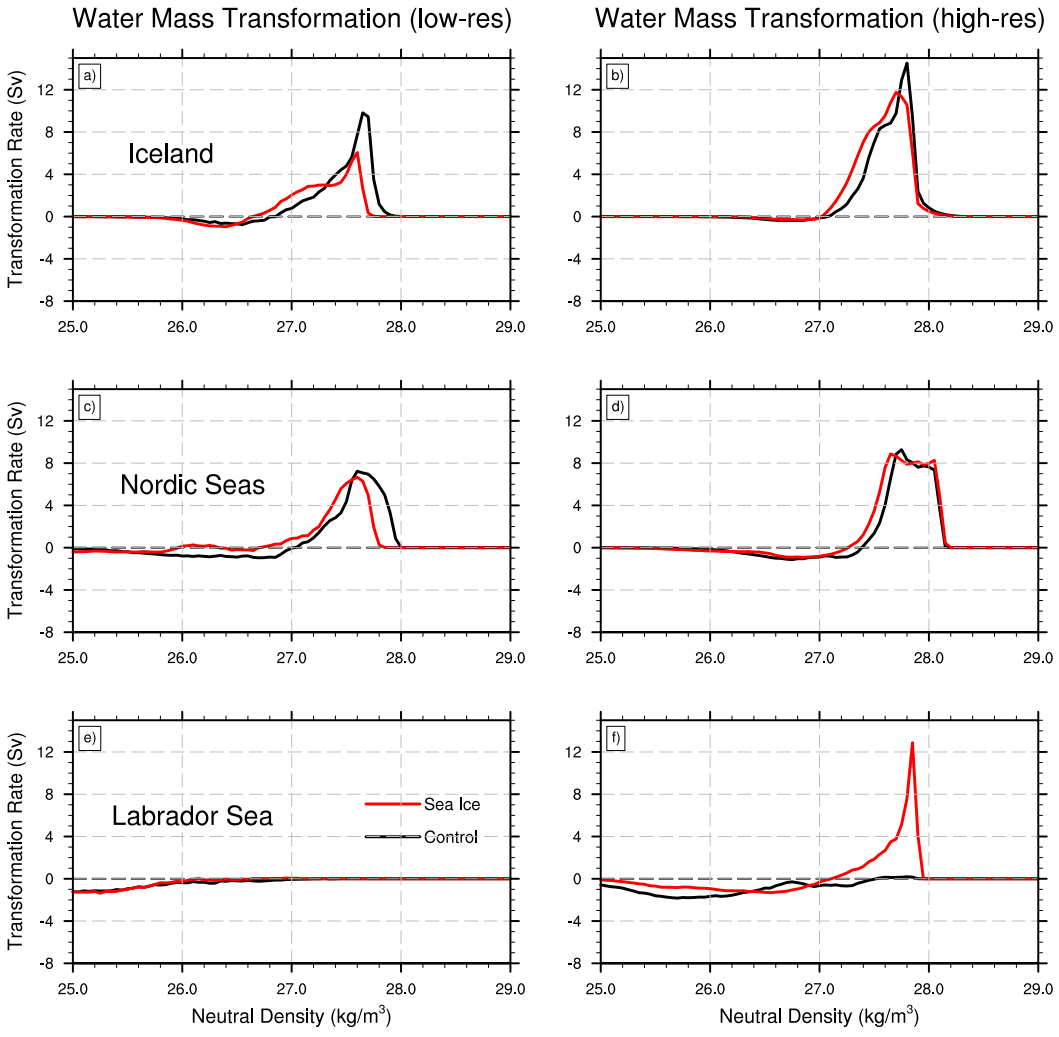

FIG. 11. WMT in different regions of the North Atlantic—(a),(b) the region to the south of Iceland, (c),(d) the Nordic seas, and (e),(f) the Labrador Sea—for the (left) low-res model and (right) high-res model. Black curves represent WMT in the control simulation, and red curves denote the last 50 years of the sea ice perturbation experiments. Note the large change in WMT in the Labrador Sea in the high-res sea ice experiment.

responses are dramatically different in these models. The AMOC in the low-res model responds to the imposed Arctic sea ice decline with a robust 30% strength reduction (~6 Sv), reaching a new quasi-equilibrium state with a weaker AMOC in roughly 100 years. In contrast, the AMOC in the high-res model undergoes a modest transient weakening (2 Sv) over the first 20–30 years, within the range of its decadal variability, followed by a recovery and slight intensification.

We argue that the contrasting AMOC behaviors in the two models can be related to the AMOC stability properties, as described by the AMOC stability indicator, which are largely controlled by the differences in the model mean states, including the basinwide mean surface freshwater fluxes and the location of NADW formation sites. Previous studies (de Vries and Weber 2005; Dijkstra 2007; Huisman et al. 2010; Liu and Liu 2013; Weijer et al. 2019) have shown that the AMOC stability indicator ΔM_{ov} is a good, albeit not perfect, diagnostic measure for whether the modeled AMOC is bistable or monostable. This AMOC stability indicator, ΔM_{ov}, reveals that the overturning circulation in the low-res control simulation *exports* freshwater out of the Atlantic catchment area, leading to a net positive large-scale salt-advection feedback that amplifies the effect of buoyancy forcing due to sea ice decline. In other words, according to the ΔM_{ov} diagnostic, the AMOC in the low-res model is less stable, which could lead to a stronger response to buoyancy perturbations. In contrast, the AMOC in the high-res model tends to *converge* freshwater into the Atlantic, with large positive values of ΔM_{ov}, creating a negative feedback to AMOC weakening and making it resilient to freshwater forcing. This negative feedback contributes to AMOC recovery despite persisting sea ice forcing.

Note that the ΔM_{ov} by itself does not explain mechanistically the different AMOC behaviors in the two models. However, ΔM_{ov} is shown to be useful as a diagnostic to understand the

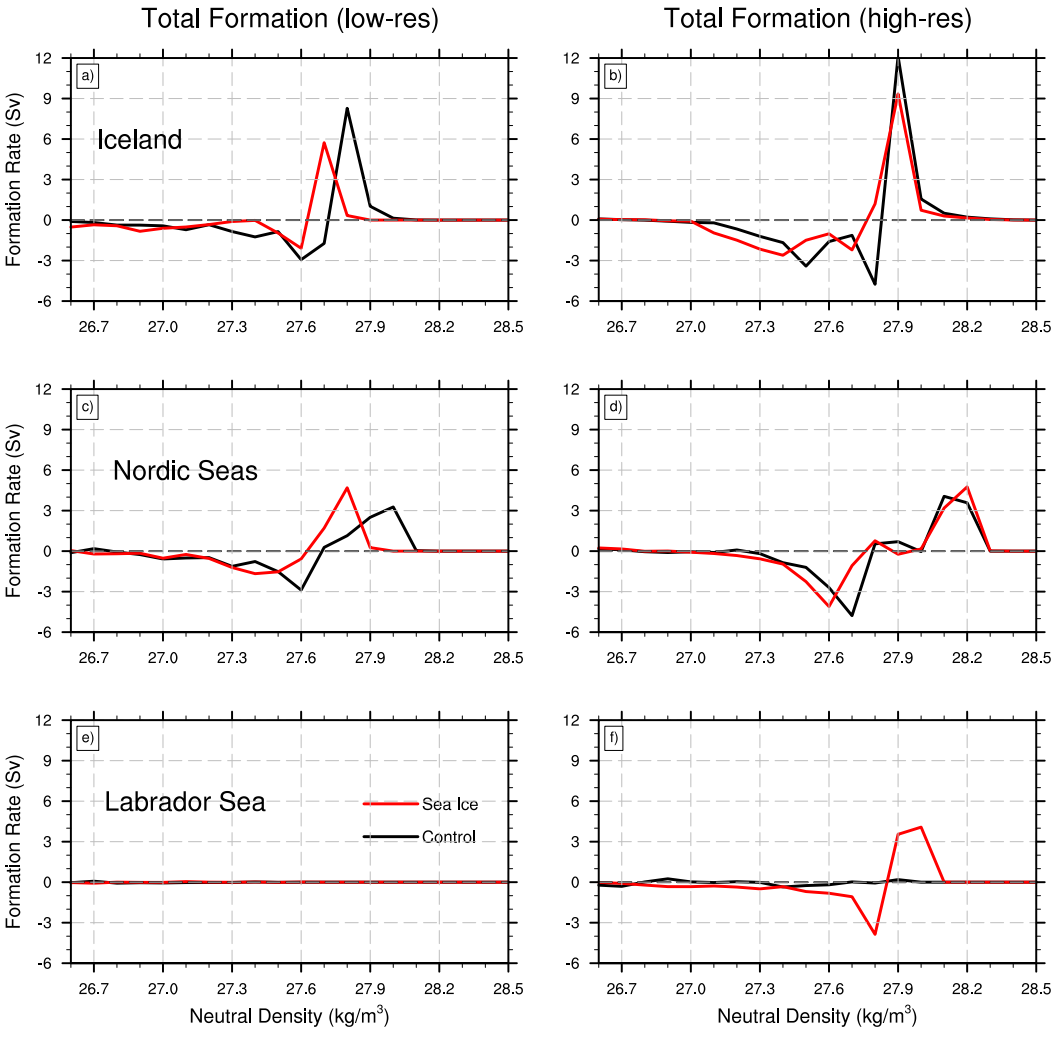

FIG. 12. As in Fig. 11, but for water mass formation rates. The formation rates, summed in 0.1 kg m^{-3} neutral density bins, represent the convergence or divergence of WMT rates with respect to density. In the control experiment both models produce deep water in the Nordic seas and the region south of Iceland but not in the Labrador Sea. Deep water starts forming in the Labrador Sea in the sea ice perturbation experiment but only in the high-resolution model.

AMOC responses in models, and in the paper we emphasize the *consistency* between the AMOC responses and ΔM_{ov} differences, but establishing a causal relationship would require future studies. While originally these ideas were introduced in the context of AMOC stability (including a bistable or monostable AMOC), here we show that they also describe the sensitivity of the system to small perturbations.

To confirm the different AMOC sensitivity to freshwater forcing implied by the stability indicator, we have performed a suite of complimentary hosing experiments. We find that, given the same, relatively weak freshwater forcing rate (0.1 Sv or smaller), the AMOC in the high-res model again shows only a small reduction of AMOC strength, while the less stable AMOC in the low-res model weakens significantly. The 0.1-Sv freshwater hosing is roughly equivalent to a freshwater forcing from the rapid initial sea ice melting: the total freshwater input from sea ice melting over the first 10 years is about 0.1 and 0.07 Sv for the two models, respectively.

There are several differences between the perturbed sea ice and hosing experiments: in the sea ice perturbation experiments, the anomalous buoyancy forcing that leads to AMOC slowdown is produced both by the freshwater input and upper-ocean warming, while the hosing experiments incorporate only the freshwater effect. In addition, the forcing in the sea ice perturbation experiments can vary with time, while the hosing experiments have a constant forcing over the entire simulation period. To address these differences, we have conducted a range of hosing experiments with different magnitude of freshwater forcing, which show the robustness of our conclusions.

Note that the sea ice perturbation experiments were designed to produce the same amount of sea ice decline by the

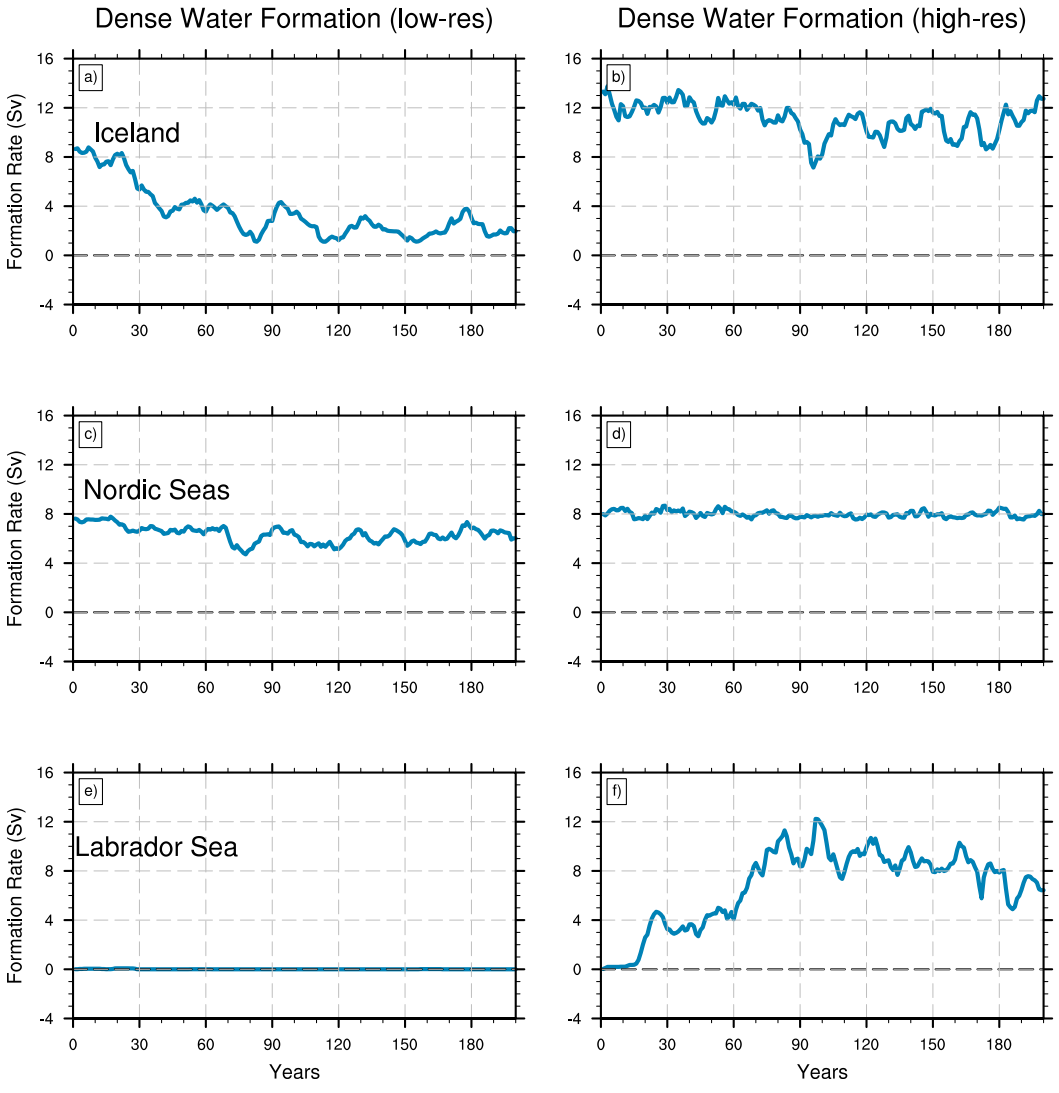

FIG. 13. Time series of net deep water formation for water denser than 27.7 kg m^{-3} in the sea ice perturbation experiments in (a),(b) the region south of Iceland, (c),(d) the Nordic seas, and (e),(f) the Labrador Sea for the (left) low-res model and (right) high-res model. The results are obtained by summing the formation rates of water for densities higher than 27.7 kg m^{-3} in Fig. 12. Note the activation of deep convection in the Labrador Sea in the high-res model (cf. Fig. 6).

end of the 200-yr simulation, but the trajectories of sea ice evolution may differ somewhat. Notably, sea ice area and volume in the high-res model decrease continuously during the ~80 years after the initiation of the perturbation, while sea ice in the low-res model shows a more abrupt change in the early decades and a rapid stabilization. This implies that the AMOC in the high-res keeps interacting with Arctic sea ice in the process of adjusting its heat and freshwater transport. The transition period of 80 years represents a time scale for the dynamic interactions involving sea ice, ocean circulations, and surface flux exchanges.

The foregoing point is that while the total freshwater input by sea ice reduction is the same, the timing of the forcing is different. In particular, the freshwater forcing from the rapid *initial* sea ice melting can be different between the two models, and the initial forcing strength may be important for igniting a particular AMOC behavior. This is partly implied by the hosing experiments, in which the AMOC response in the sea ice experiments is best replicated with a 0.1-Sv hosing rate in the low-res but with a 0.05-Sv hosing rate in the high-res. Yet, this does not affect our conclusions about AMOC stability and their impact on AMOC response to freshwater forcing, which can be substantiated by juxtaposing the two models' contrasting AMOC behavior to the same freshwater forcing.

In addition, the Arctic sea ice is a highly dynamic system that has intricate relationships with ocean convection and overturning. The decline of sea ice and the associated changes of its

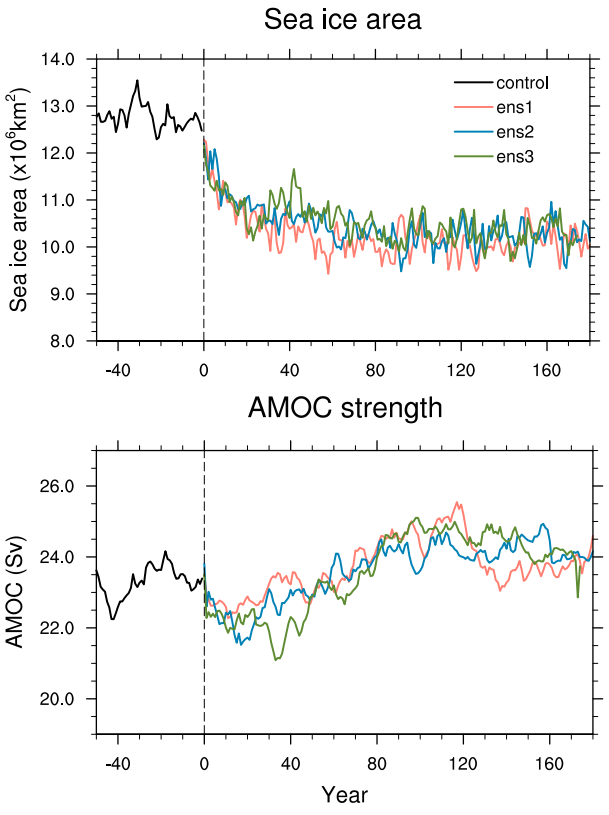

FIG. 14. Simulated (a) Arctic sea ice total area and (b) AMOC strength as a function of time across different members of the high-res experiment. Black curves show the control. The red, blue, and green curves show results from the sea ice perturbation simulations wherein the standard deviation parameter of the optical properties of bare ice and ponded ice (R_ice and R_pnd) is modified to −5, −4, and −3, respectively. These slightly different high-res perturbation experiments are treated as a small ensemble. Note the robust 1–2-Sv weakening of the AMOC lasting from several decades to about a half century.

seasonality can restructure the spatial patterns of buoyancy forcing in the subpolar region. While the bulk response of sea ice reduction is an anomalous input of freshwater forcing, the melting can in fact expose subarctic regions to stronger winds and evaporation, possibly leading to enhanced ocean convection at some locations (Fig. 6). When amplified by the salt-advection feedback, this effect can help sustain the AMOC. In fact, our analysis of water mass transformation and the NADW formation in different regions of the subpolar North Atlantic reveals that, in the sea ice perturbation experiments, the AMOC in the high-res model can maintain and possibly increase deep water formation by activating deep convection in the Labrador Sea and the broad region south of Greenland (absent in the control simulation). This becomes a major factor in the diverging AMOC behaviors in the two modes. Thus, the interplay between how different deep water formation sites respond to the forcing is critical to whether the AMOC continues to weaken or ultimately recovers.

In turn, these changes in deep convection reflect the differences in the AMOC stability characteristics. In particular, the development of deep convection in the Labrador Sea region and south of Greenland in the high-res model is possible because of the strong negative basin-scale salt advection feedback: the accumulation of salt in the North Atlantic with the weakening of the AMOC amplifies surface salinity anomalies in the Labrador Sea to a degree sufficient for the development of deep convection there.

Our study is an effort to better understand the AMOC behavior and how it may respond to a changing climate with a declining Arctic sea ice cover. A question arises as to which type of AMOC response would occur in nature: a strong AMOC weakening that leads to a new equilibrium state or a modest transient weakening followed by full recovery? Perhaps it is the former type of response since the low-resolution model is more realistic in that it has a better representation of the Atlantic salinity distribution, the AMOC mean strength and AMOC stability. In fact, computations with an ocean adjoint model (Sévellec et al. 2017) and experiments with several other coupled models, such as GFDL CM3 (Sun et al. 2018) and CNRM-CM5 (Oudar et al. 2017), agree with the low-res results here. Simulations with CCSM4, however—a model similar to our high-res model—reproduce the latter type of response (Blackport and Kushner 2016; Wang et al. 2018). Thus, correctly representing both sea ice dynamic and AMOC stability properties in GCMs is critical to predicting future AMOC changes.

Note that, despite the described differences, even in the high-res ensemble (which most likely has an overly stable AMOC) the decreasing Arctic sea ice still results in a robust AMOC weakening of up to 2 Sv (Fig. 14) lasting for about a half century, which is particularly relevant to the ongoing climate change.

Acknowledgments. This research was supported by grants to author Fedorov from NSF (AGS-0163807, OPP-1741841) and by the Guggenheim Fellowship. Additional support is provided through the ARCHANGE project (ANR-18-MPGA-0001; France). Author Li is also supported by the Regional and Global Climate Modeling Program (RGCM) of the U.S. Department of Energy's Office of Biological & Environmental Research (BER) via National Science Foundation IA 1844590. Author Liu is supported by the Regents' Faculty Fellowship and also by the Alfred P. Sloan Foundation as a Research Fellow. We thank Kaylea Nelson for her help in setting up the computational environment and acknowledge computational support from the Yale HPC Center. The National Center for Atmospheric Research is sponsored by the National Science Foundation.

Data availability statement. The observational record for sea ice area is provided by the National Snow and Ice Data Center (NSIDC) and is based on gridded brightness temperatures from the Defense Meteorological Satellite Program series of the Special Sensor Microwave Imager and the Special Sensor Microwave Imager/Sounder. The data are available online (https://nsidc.org/data/NSIDC-0192/versions/3). Sea ice volume from Pan-Arctic Ice Ocean Modeling and Assimilation System (PIOMAS) can be accessed at http://psc.apl.uw.edu/research/projects/arctic-sea-ice-volume- anomaly/data/. The ORAS4 ocean reanalysis data can be accessed at https://www.ecmwf.int/en/research/climate-reanalysis/ocean-reanalysis. The high-res control simulation is obtained from NCAR model

case "b40.1850.track1.2deg.003" and can be obtained from the Earth System Grid (https://www.earthsystemgrid.org/dataset/ucar.cgd.ccsm4.joc.b40.1850.track1.1deg.006.html). All model data used in this paper are stored at Zenodo (https://doi.org/10.5281/zenodo.3626238).

REFERENCES

Balmaseda, M. A., K. Mogensen, and A. T. Weaver, 2013: Evaluation of the ECMWF Ocean Reanalysis System ORAS4. *Quart. J. Roy. Meteor. Soc.*, **139**, 1132–1161, https://doi.org/10.1002/qj.2063.

Blackport, R., and P. J. Kushner, 2016: The transient and equilibrium climate response to rapid summertime sea ice loss in CCSM4. *J. Climate*, **29**, 401–417, https://doi.org/10.1175/JCLI-D-15-0284.1.

Booth, B. B. B., N. J. Dunstone, P. R. Halloran, T. Andrews, and N. Bellouin, 2012: Aerosols implicated as a prime driver of twentieth-century North Atlantic climate variability. *Nature*, **484**, 228–232, https://doi.org/10.1038/nature10946.

Broecker, W. S., G. Bond, M. Klas, G. Bonani, and W. Wolfli, 1990: A salt oscillator in the glacial Atlantic? 1. The concept. *Paleoceanography*, **5**, 469–477, https://doi.org/10.1029/PA005i004p00469.

Bryan, F., 1986: High-latitude salinity effects and interhemispheric thermohaline circulations. *Nature*, **323**, 301–304, https://doi.org/10.1038/323301a0.

——, M. W. Hecht, and R. D. Smith, 2007: Resolution convergence and sensitivity studies with North Atlantic circulation models. Part I: The western boundary current system. *Ocean Modell.*, **16**, 141–159, https://doi.org/10.1016/j.ocemod.2006.08.005.

Bryden, H. L., B. A. King, and G. D. McCarthy, 2011: South Atlantic overturning circulation at 24°S. *J. Mar. Res.*, **69**, 38–55, https://doi.org/10.1357/002224011798147633.

Buckley, M. W., and J. Marshall, 2016: Observations, inferences, and mechanisms of the Atlantic meridional overturning circulation: A review. *Rev. Geophys.*, **54**, 5–63, https://doi.org/10.1002/2015RG000493.

Caesar, L., S. Rahmstorf, A. Robinson, G. Feulner, and V. Saba, 2018: Observed fingerprint of a weakening Atlantic Ocean overturning circulation. *Nature*, **556**, 191–196, https://doi.org/10.1038/s41586-018-0006-5.

Danabasoglu, G., and Coauthors, 2014: North Atlantic simulations in coordinated ocean-ice reference experiments phase II (CORE-II). Part I: Mean states. *Ocean Modell.*, **73**, 76–107, https://doi.org/10.1016/j.ocemod.2013.10.005.

Dansgaard, W., and Coauthors, 1993: Evidence for general instability of past climate from a 250-kyr ice-core record. *Nature*, **364**, 218–220, https://doi.org/10.1038/364218a0.

Day, J. J., J. C. Hargreaves, J. D. Annan, and A. Abe-Ouchi, 2012: Sources of multi-decadal variability in Arctic sea ice extent. *Environ. Res. Lett.*, **7**, 034011, https://doi.org/10.1088/1748-9326/7/3/034011.

de Vries, P., and S. L. Weber, 2005: The Atlantic freshwater budget as a diagnostic for the existence of a stable shut down of the meridional overturning circulation. *Geophys. Res. Lett.*, **32**, L09606, https://doi.org/10.1029/2004GL021450.

Dijkstra, H. A., 2007: Characterization of the multiple equilibria regime in a global ocean model. *Tellus*, **59A**, 695–705, https://doi.org/10.1111/j.1600-0870.2007.00267.x.

Drijfhout, S. S., S. L. Weber, and E. van der Swaluw, 2011: The stability of the MOC as diagnosed from model projections for pre-industrial, present and future climates. *Climate Dyn.*, **37**, 1575–1586, https://doi.org/10.1007/s00382-010-0930-z.

Gent, P. R., 2018: A commentary on the Atlantic meridional overturning circulation stability in climate models. *Ocean Modell.*, **122**, 57–66, https://doi.org/10.1016/j.ocemod.2017.12.006.

Gregory, J. M., and Coauthors, 2005: A model intercomparison of changes in the Atlantic thermohaline circulation in response to increasing atmospheric CO_2 concentration. *Geophys. Res. Lett.*, **32**, L12703, https://doi.org/10.1029/2005GL023209.

Groeskamp, S., S. M. Griffies, D. Iudicone, R. Marsh, A. J. G. Nurser, and J. D. Zika, 2019: The water mass transformation framework for ocean physics and biogeochemistry. *Annu. Rev. Mar. Sci.*, **11**, 271–305, https://doi.org/10.1146/annurev-marine-010318-095421.

Hu, A., B. L. Otto-Bliesner, G. A. Meehl, W. Han, C. Morrill, E. C. Brady, and B. Briegleb, 2008: Response of thermohaline circulation to freshwater forcing under present-day and LGM conditions. *J. Climate*, **21**, 2239–2258, https://doi.org/10.1175/2007jcli1985.1

Huisman, S. E., M. den Toom, H. A. Dijkstra, and S. Drijfhout, 2010: An indicator of the multiple equilibria regime of the Atlantic meridional overturning circulation. *J. Phys. Oceanogr.*, **40**, 551–567, https://doi.org/10.1175/2009JPO4215.1.

Hurrell, J. W., and Coauthors, 2013: The Community Earth System Model: A framework for collaborative research. *Bull. Amer. Meteor. Soc.*, **94**, 1339–1360, https://doi.org/10.1175/BAMS-D-12-00121.1.

Jackson, L. C., R. S. Smith, and R. A. Wood, 2017: Ocean and atmosphere feedbacks affecting AMOC hysteresis in a GCM. *Climate Dyn.*, **49**, 173–191, https://doi.org/10.1007/s00382-016-3336-8.

Kostov, Y., K. C. Armour, and J. Marshall, 2014: Impact of the Atlantic meridional overturning circulation on ocean heat storage and transient climate change. *Geophys. Res. Lett.*, **41**, 2108–2116, https://doi.org/10.1002/2013GL058998.

Liu, W., and Z. Liu, 2013: A diagnostic indicator of the stability of the Atlantic meridional overturning circulation in CCSM3. *J. Climate*, **26**, 1926–1938, https://doi.org/10.1175/JCLI-D-11-00681.1.

——, ——, and E. C. Brady, 2014: Why is the AMOC monostable in coupled general circulation models? *J. Climate*, **27**, 2427–2443, https://doi.org/10.1175/JCLI-D-13-00264.1.

——, S.-P. Xie, Z. Liu, and J. Zhu, 2017: Overlooked possibility of a collapsed Atlantic meridional overturning circulation in warming climate. *Sci. Adv.*, **3**, e1601666, https://doi.org/10.1126/sciadv.1601666.

——, A. Fedorov, and F. Sévellec, 2018: The mechanisms of the Atlantic meridional overturning circulation slowdown induced by Arctic sea ice decline. *J. Climate*, **32**, 977–996, https://doi.org/10.1175/JCLI-D-18-0231.1.

——, ——, S.-P. Xie, and S. Hu, 2020: Climate impacts of a weakened Atlantic meridional overturning circulation in a warming climate. *Sci. Adv.*, **6**, eaaz4876, https://doi.org/10.1126/sciadv.aaz4876.

Lynch-Stieglitz, J., 2016: The Atlantic meridional overturning circulation and abrupt climate change. *Annu. Rev. Mar. Sci.*, **9**, 83–104, https://doi.org/10.1146/ANNUREV-MARINE-010816-060415.

Mahajan, S., R. Zhang, and T. L. Delworth, 2011: Impact of the Atlantic meridional overturning circulation (AMOC) on Arctic surface air temperature and sea ice variability. *J. Climate*, **24**, 6573–6581, https://doi.org/10.1175/2011JCLI4002.1.

Manabe, B. S., and R. J. Stouffer, 1999: Are two modes of thermohaline circulation stable? *Tellus*, **51A**, 400–411, https://doi.org/10.3402/tellusa.v51i3.13461.

Marshall, J., A. Donohoe, D. Ferreira, and D. McGee, 2014: The ocean's role in setting the mean position of the inter-tropical convergence zone. *Climate Dyn.*, **42**, 1967–1979, https://doi.org/10.1007/s00382-013-1767-z.

Mecking, J. V., S. S. Drijfhout, L. C. Jackson, and M. B. Andrews, 2017: The effect of model bias on Atlantic freshwater transport and implications for AMOC bi-stability. *Tellus A*, **69A**, 1299910, https://doi.org/10.1080/16000870.2017.1299910.

Miles, M. W., D. V. Divine, T. Furevik, E. Jansen, M. Moros, and A. E. J. Ogilvie, 2014: A signal of persistent Atlantic multidecadal variability in Arctic sea ice. *Geophys. Res. Lett.*, **41**, 463–469, https://doi.org/10.1002/2013GL058084.

Oudar, T., E. Sanchez-Gomez, F. Chauvin, J. Cattiaux, L. Terray, and C. Cassou, 2017: Respective roles of direct GHG radiative forcing and induced Arctic sea ice loss on the Northern Hemisphere atmospheric circulation. *Climate Dyn.*, **49**, 3693–3713, https://doi.org/10.1007/s00382-017-3541-0.

Prange, M., G. Lohmann, and A. Paul, 2003: Influence of vertical mixing on the thermohaline hysteresis: Analyses of an OGCM. *J. Phys. Oceanogr.*, **33**, 1707–1721, https://doi.org/10.1175/2389.1.

Rahmstorf, S., 1996: On the freshwater forcing and transport of the Atlantic thermohaline circulation. *Climate Dyn.*, **12**, 799–811, https://doi.org/10.1007/s003820050144.

——, and Coauthors, 2005: Thermohaline circulation hysteresis: A model intercomparison. *Geophys. Res. Lett.*, **32**, L23605, https://doi.org/10.1029/2005GL023655.

——, J. E. Box, G. Feulner, M. E. Mann, A. Robinson, S. Rutherford, and E. J. Schaffernicht, 2015: Exceptional twentieth-century slowdown in Atlantic Ocean overturning circulation. *Nat. Climate Change*, **5**, 475–480, https://doi.org/10.1038/nclimate2554.

Sévellec, F., A. V. Fedorov, and W. Liu, 2017: Arctic sea-ice decline weakens the Atlantic meridional overturning circulation. *Nat. Climate Change*, **7**, 604–610, https://doi.org/10.1038/nclimate3353.

Shields, C. A., D. A. Bailey, G. Danabasoglu, M. Jochum, J. T. Kiehl, S. Levis, and S. Park, 2012: The low-resolution CCSM4. *J. Climate*, **25**, 3993–4014, https://doi.org/10.1175/JCLI-D-11-00260.1.

Sijp, W. P., and M. H. England, 2006: Sensitivity of the Atlantic thermohaline circulation and its stability to basin-scale variations in vertical mixing. *J. Climate*, **19**, 5467–5478, https://doi.org/10.1175/JCLI3909.1.

Smeed, D. A., and Coauthors, 2018: The North Atlantic Ocean is in a state of reduced overturning. *Geophys. Res. Lett.*, **45**, 1527–1533, https://doi.org/10.1002/2017GL076350.

Stommel, H., 1961: Thermohaline convection with two stable regimes of flow. *Tellus*, **13**, 224–230, https://doi.org/10.1111/j.2153-3490.1961.tb00079.x

Stouffer, R. J., and Coauthors, 2006: Investigating the causes of the response of the thermohaline circulation to past and future climate changes. *J. Climate*, **19**, 1365–1387, https://doi.org/10.1175/JCLI3689.1.

Sun, L., M. Alexander, and C. Deser, 2018: Evolution of the global coupled climate response to Arctic sea ice loss during 1990–2090 and its contribution to climate change. *J. Climate*, **31**, 7823–7843, https://doi.org/10.1175/JCLI-D-18-0134.1.

Thomas, M. D., and A. V. Fedorov, 2019: Mechanisms and impacts of a partial AMOC recovery under enhanced freshwater forcing. *Geophys. Res. Lett.*, **46**, 3308–3316, https://doi.org/10.1029/2018GL080442.

Trenberth, K. E., and J. M. Caron, 2001: Estimates of meridional atmosphere and ocean heat transports. *J. Climate*, **14**, 3433–3443, https://doi.org/10.1175/1520-0442(2001)014<3433:EOMAAO>2.0.CO;2.

Wang, K., C. Deser, L. Sun, and R. A. Tomas, 2018: Fast response of the tropics to an abrupt loss of Arctic sea ice via ocean dynamics. *Geophys. Res. Lett.*, **45**, 4264–4272, https://doi.org/10.1029/2018GL077325.

Weaver, A. J., and Coauthors, 2012: Stability of the Atlantic meridional overturning circulation: A model intercomparison. *Geophys. Res. Lett.*, **39**, 2012GL053763, https://doi.org/10.1029/2012GL053763.

Weijer, W., and Coauthors, 2019: Stability of the Atlantic meridional overturning circulation: A review and synthesis. *J. Geophys. Res. Oceans*, **124**, 5336–5375, https://doi.org/10.1029/2019JC015083.

Yin, J., and R. J. Stouffer, 2007: Comparison of the stability of the Atlantic thermohaline circulation in two coupled atmosphere–ocean general circulation models. *J. Climate*, **20**, 4293–4315, https://doi.org/10.1175/JCLI4256.1.

Zhang, R., 2015: Mechanisms for low-frequency variability of summer Arctic sea ice extent. *Proc. Natl. Acad. Sci. USA*, **112**, 4570–4575, https://doi.org/10.1073/pnas.1422296112.